

Electronic Supplementary Information

Multifunctionality of Lanthanum-Strontium Manganite Nanopowder

Ziyu Wei^a, A.V. Pashchenko^{a,b,c,d,*}, N.A. Liedienov^{a,b,*}, I.V. Zatovsky^e, D.S. Butenko^e, Qunjun Li^a,
I.V. Fesykh^f, V.A. Turchenko^{b,g}, E.E. Zubov^h, P.Yu. Polynchuk^c, V.G. Pogrebnyak^d,
V.M. Poroshinⁱ, G.G. Levchenko^{a,b,*}

^aState Key Laboratory of Superhard Materials, International Center of Future Science, Jilin University, 130012 Changchun, China

^bDonetsk Institute for Physics and Engineering named after O.O. Galkin, NASU, 03028 Kyiv, Ukraine

^cInstitute of Magnetism, NASU and MESU, 03142 Kyiv, Ukraine

^dIvano-Frankivsk National Technical University of Oil and Gas, MESU, 76019 Ivano-Frankivsk, Ukraine

^eCollege of Physics, Jilin University, 130012 Changchun, China

^fTaras Shevchenko National University of Kyiv, 01030 Kyiv, Ukraine

^gFrank Laboratory of Neutron Physics, Joint Institute for Nuclear Research, 141980 Dubna, Russia

^hG.V. Kurdyumov Institute for Metal Physics, 03142 Kyiv, Ukraine

ⁱInstitute of Physics, NASU, 03028 Kyiv, Ukraine

*Corresponding author

E-mail address:

alpash@ukr.net (A.V. Pashchenko)

nikita.ledenev.ssp@gmail.com (N.A. Liedienov)

g-levch@ukr.net (G.G. Levchenko)

ESI1

Determination of the size of coherent scattering region and X-ray density in the

La_{0.6}Sr_{0.4}MnO₃ nanopowder

The size of the coherent scattering region D^{CSR} was determined using the Scherrer method.

The average size D^{CSR} in the La_{0.6}Sr_{0.4}MnO₃ nanopowder is related to the dimensional broadening of β for diffraction reflection (012) according to the Scherrer equation [1]:

$$D = K\lambda / \beta \cos\theta, \quad (\text{S1})$$

where D is the size of scattering crystallites in nm; $\lambda = 0.15406$ nm is the wavelength of X-ray radiation; $K = 0.9$ is a constant that depends on the method for determining the line broadening and crystal shape; β is the width of the intensity distribution curve at half the height of the maximum of the reflex in radians; θ is the diffraction angle in degrees. The true integral width of peak was

calculated using the Warren formula [2]: $\beta = \sqrt{\beta_{\text{exp}}^2 - \beta_0^2}$, where β_{exp} is the total peak width of the measured sample at half maximum intensity (FWHM) in radians; β_0 is the instrumental broadening

of the diffraction line, which depends on the structural features of the diffractometer. The resolution function of the diffractometer β_0 was determined in a separate experiment from the diffraction pattern for the standard. A single crystal silicon standard (JCPDS89-2955) was used as a standard.

The average size of the D^{CSR} was obtained using the Gaussian function while approximating the experimental values of the intensity of the diffraction maximum with a Bragg angle of $2\theta \approx 22.8^\circ$ and taking into account all the experimental parameters in equation (S1) (see Table S1).

Table S1

The experimental parameters in the Equation (S1), and the average size of the coherent scattering regions D_{CSR} for the $\text{La}_{0.6}\text{Sr}_{0.4}\text{MnO}_3$ nanopowder with different annealing temperatures t_{ann} .

$t_{\text{ann}}, ^\circ\text{C}$	2θ , degree	β , radian	$\cos\theta$	λ , nm	K	D_{012} , nm
700	22.86	0.0088	0.980168	0.15406	0.9	16±1
750	22.80	0.0081	0.980271	0.15406	0.9	17±1
800	22.88	0.0071	0.980133	0.15406	0.9	20±1
850	22.866	0.0054	0.980157	0.15406	0.9	26±1
900	22.86	0.0047	0.980168	0.15406	0.9	30±1

ESI2

The refinement of crystal structure of single-phase $\text{La}_{0.6}\text{Sr}_{0.4}\text{MnO}_3$ nanopowders with $t_{\text{ann}} = 800, 850$ and 900°C by the Rietveld analysis

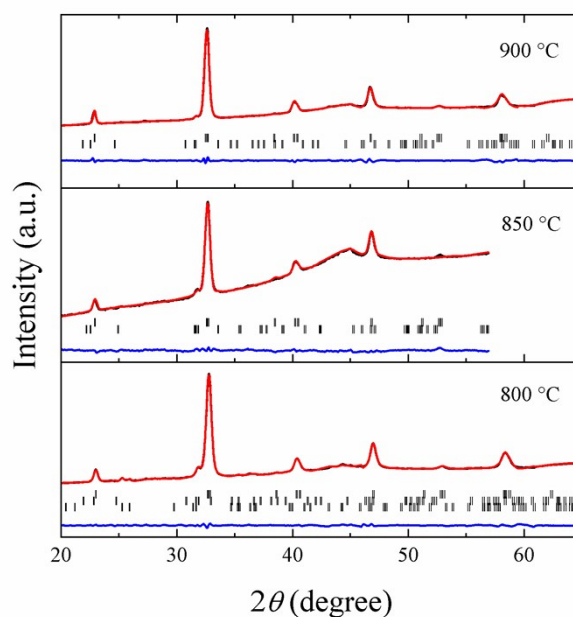


Fig. S1. X-ray diffraction patterns of the $\text{La}_{0.6}\text{Sr}_{0.4}\text{MnO}_3$ nanopowders ($t_{\text{ann}} = 800, 850$, and 900°C) measured at room temperature and fitted using the Rietveld method. The experimental and calculated values (black and red curves), and difference curve (blue line) normalized to a statistical

error are presented. Vertical bars are calculated positions of diffraction peaks corresponding to the $R\bar{3}c$ space group.

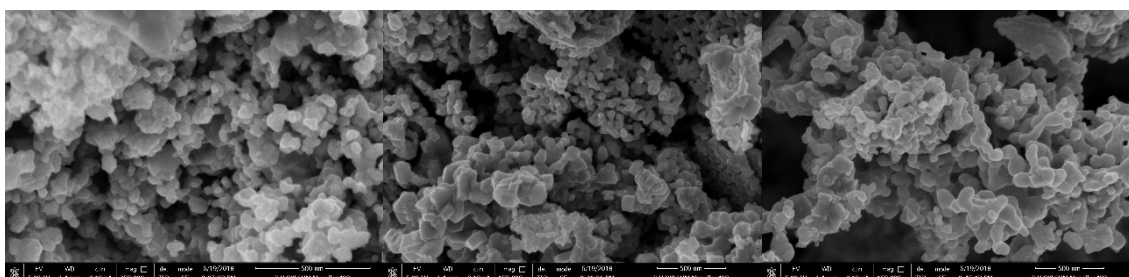
Table S2

Phase composition and structural properties of single-phase $\text{La}_{0.6}\text{Sr}_{0.4}\text{MnO}_3$ nanopowders ($t_{\text{ann}} = 800, 850$ and 900 °C) according to Rietveld analysis (a, b, c , and V are parameters and unit cell volume; Z is the number of formula units per unit cell; Fract. is the phase amount).

t_{ann} , °C	Parameter	Phase No. 1	Phase No. 2	Phase No. 3
		$\text{La}_{0.6}\text{Sr}_{0.4}\text{MnO}_3$	$\text{La}_{0.6}\text{Sr}_{0.4}\text{MnO}_3$	SrCO_3
800	SG	$R\bar{3}c$	$Pbnm$	$Pnma$
	a , Å	5.48469 (0.00022)	5.65629 (0.00303)	6.00789 (0.00384)
	b , Å		5.80618 (0.00358)	5.09134 (0.00234)
	c , Å	13.32763 (0.00102)	7.79333 (0.00360)	8.39022 (0.00419)
	V , Å ³	347.207 (0.033)	255.944 (0.240)	256.642 (0.239)
	Z	6	4	4
	Fract., %	99.15 (0.31)	0.72 (0.00)	0.13 (0.00)
850	SG	$R\bar{3}c$	$Pbnm$	
	a , Å	5.49992 (0.00076)	5.65629 (0.00000)	
	b , Å		5.67838 (0.01024)	
	c , Å	13.38241 (0.00346)	7.89266 (0.01012)	
	V , Å ³	350.573(0.114)	253.501 (0.561)	—
	Z	6	4	
	Fract., %	99.83(0.89)	0.17(0.01)	
900	SG	$R\bar{3}c$	$Pbnm$	
	a , Å	5.51159 (0.00022)	5.82043 (0.01038)	
	b , Å		5.67838 (0.00000)	
	c , Å	13.39703 (0.00104)	7.89369 (0.01014)	
	V , Å ³	352.447(0.034)	260.891 (0.574)	—
	Z	6	4	
	Fract., %	99.93(0.95)	0.07(0.01)	

ESI3

Determination of the particle size distribution function in the $\text{La}_{0.6}\text{Sr}_{0.4}\text{MnO}_3$ nanopowder



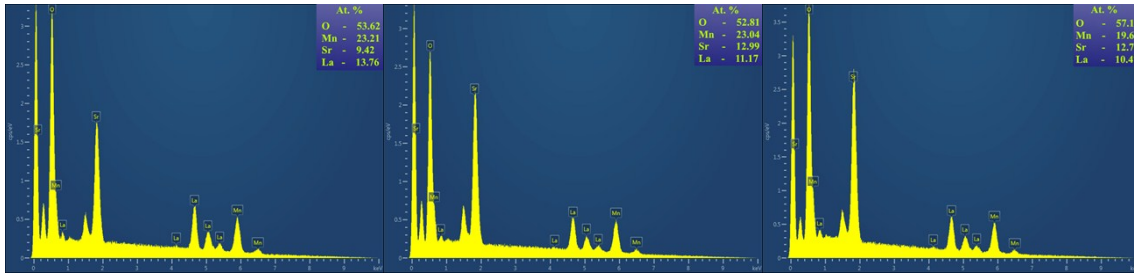


Fig. S2. SEM images (top) and EDS of chemical composition (bottom) for the LSMO-800 (left), LSMO-850 (center) and LSMO-900 (right) nanopowders.

According to the EDS spectra, filling the *A*-position with lanthanum and strontium, as well as *B*-position with manganese corresponds to the stoichiometric ratio $A(\text{La}):A(\text{Sr}):B(\text{Mn}) = 0.6:0.4:1$ only for the LSMO-800 powder. As it can be seen from the pseudobinary $\text{La}_2\text{O}_3\text{-Mn}_2\text{O}_3$ phase diagram [3], other minor phases can form in addition to the primary perovskite-like phase at high annealing temperatures from 700 to 1500 °C.

The appearance of non-stoichiometry defects in single-phase manganites with a perovskite structure is associated with the appearance of anionic $V^{(a)}$ and cationic $V^{(c)}$ vacancies at high sintering and annealing temperatures. According to the defect formation mechanism [4-5], the appearance of $V^{(a)}$ vacancies occurs upon heating of the samples and is caused by thermal dissociation of oxygen. The appearance of $V^{(c)}$ vacancies occurs upon cooling of the samples and is due to the greater mobility of the cationic sublattice. The result of the heating process is that the real perovskite structure contains both $V^{(a)}$ and $V^{(c)}$ vacancies. Moreover, the molar formula of the real LSMO perovskite takes the form $[\text{La}, \text{Sr}, V^{(c)}]_A \{ \text{Mn}, V^{(c)} \}_B \text{O}_{3-\delta} V_\delta^{(a)}$.

While analyzing the phase state and finding the molar formulas of the real $\text{La}_{0.6}\text{Sr}_{0.4}\text{MnO}_3$ structure with using EDS spectra, it is necessary to take into account that the oxygen content in the samples during their annealing in air can vary depending on the annealing temperature and the “heating/cooling” mode. Only the ratio of *A*- and *B*-cations remains constant, but only if there is no volatility in the cation sublattice. Therefore, while refining the chemical composition, the only independent parameter is the ratio $A(\text{La}):A(\text{Sr}):B(\text{Mn})$, where *A* and *B* are the filling factors of *A*- and *B*-positions with La, Sr, and Mn ions.

The analysis of the chemical and phase composition in the LSMO-800 powder was carried out taking into account the following conditions:

- (i) the EDS spectra can be associated not only with the primary LSMO perovskite phase, but also with minor Mn_3O_4 , $(\text{La}, \text{Sr})\text{Mn}_2\text{O}_4$, La_2O_3 , $\text{La}(\text{OH})_3$, and $(\text{La}, \text{Sr})_2\text{MnO}_4$ phases [6];
- (ii) the EDS identifies two minor Mn_3O_4 and $(\text{La}, \text{Sr})\text{Mn}_2\text{O}_4$ phases for $A/B < 1$ [6];
- (iii) the La_2O_3 , $(\text{La}, \text{Sr})_2\text{MnO}_4$ and $(\text{La}, \text{Sr})_3\text{Mn}_2\text{O}_7$ minor phases present are for $A/B > 1$ [6];
- (iv) the formation of a stable perovskite structure without the content of the minor phases is observed in the range $B/(A+B) = 0.475\text{--}0.524$ [3];
- (v) in $\text{La}_{1-x}\text{Sr}_x\text{MnO}_3$ perovskite, the unit cell volume V_{H} in the hexagonal setup depends on the strontium content and satisfies the linear dependence $V(\text{\AA}^3) = 357.51 - 25.884 \cdot x$ for $0.1 < x < 0.7$ [6];
- (vi) the evolution of the unit cell volume of non-stoichiometric $\text{La}_{0.6}\text{Sr}_{0.4}\text{MnO}_{3-\delta}$ perovskite has the form $V_{\text{R}}(\text{\AA}^3) = 19.69 \cdot \delta + 232.78$ for the hexagonal $R\bar{3}c$ structure in the rhombohedral setup and $V_{\text{Orth}}(\text{\AA}^3) = 80.35 \cdot \delta + 231.68$ for the orthorhombic $Pbnm$ structure [7];
- (vii) in non-stoichiometric $\text{LaMnO}_{3-\delta}$ perovskite with $A/B = 1$, the unit cell volume V with $Z = 4$ depends on δ according to the dependence $V_{\text{R}}(\text{\AA}^3) = 244.86 - 68.81 \cdot \delta$ [3].

Using the EDS spectra (see Fig. S2) and the Rietveld analysis (see Table S2), $x = 0.398$ for Sr from condition (v) and $\delta = 0.066$ for $\text{V}^{(a)}$ from condition (vi) were determined. The stoichiometric ratio of $A(\text{La}):A(\text{Sr}):B(\text{Mn}) = 13.76:9.42:23.3$ and the found value $x = 0.398$ made it possible to obtain molar contents of $A(\text{La}) = 0.581$ and $B(\text{Mn}) = 0.985$ for La and Mn, respectively. The values of $A(\text{La})$, $A(\text{Sr})$, $B(\text{Mn})$, A/B , and $B/(A+B)$ (see Table S3) confirm the absence of volatility of the cationic sublattice in the LSMO-800 and correspond to the stable formation region of a perovskite structure without the minor phases (see condition (iv)). Using the electroneutrality principle, it was possible to find the molar formula $[\text{La}_{0.58}^{3+}\text{Sr}_{0.40}^{2+}\text{V}_{0.02}^{(c)}]_A \{ \text{Mn}_{0.60}^{3+}\text{Mn}_{0.38}^{4+}\text{V}_{0.02}^{(c)} \}_B \text{O}_{2.93}^{2-}\text{V}_{0.07}^{(a)}$ of a real $R\bar{3}c$ perovskite structure for the LSMO-800 powder.

Similarly, the molar formula $[\text{La}_{0.60}^{3+}\text{Sr}_{0.40}^{2+}]_A \{ \text{Mn}_{0.60}^{3+} \}_B \text{O}_{2.80}^{2-}\text{V}_{0.20}^{(a)}$ for the $Pbnm$ structure (Phase No. 2 in the LSMO-800 powder) was obtained. For that, condition (vii) was used additionally that

was associated with a high concentration of $V^{(a)}$ vacancies. The decrease in the charge of the anion sublattice with increasing δ occurs due to the transition of $Mn^{4+} \rightarrow Mn^{3+}$ until $\delta < 0.2$. At $\delta = 0.2$, all manganese in the $La_{0.6}Sr_{0.4}MnO_{3-\delta}$ transforms in the trivalent state.

Table S3

The unit cell volume of the $R\bar{3}c$ structure in the hexagonal (V_H) and rhombohedral (V_R) installation, the occupancy ratios of A - and B -positions with La, Sr, and Mn ions and the deviation from oxygen stoichiometry (δ) in the LSMO-800 powder.

Structure	$V_H, \text{\AA}^3$	$V_R, \text{\AA}^3$	$A(\text{La})$	$A(\text{Sr})$	$B(\text{Mn})$	δ	A/B	$B/(A+B)$
$R\bar{3}c$	347.206	231.471	0.581	0.398	0.985	0.066	0.995	0.501

Thus, the molar formula of the real $R\bar{3}c$ structure is $[La_{0.58}^{3+}Sr_{0.40}^{2+}V_{0.02}^{(c)}]_A \{Mn_{0.60}^{3+}Mn_{0.38}^{4+}V_{0.02}^{(c)}\}_B O_{2.93}^{2-}V_{0.07}^{(a)}$ and contains small amount of non-stoichiometry defects in the form of cationic $V^{(c)}$ and anionic $V^{(a)}$ vacancies. The molar formula of the real $Pbnm$ structure is $[La_{0.60}^{3+}Sr_{0.40}^{2+}]_A \{Mn_{0.60}^{3+}\}_B O_{2.80}^{2-}V_{0.20}^{(a)}$ with a high concentration of anionic $V^{(a)}$ vacancies. It should be also noted that this orthorhombic $Pbnm$ structure of the LSMO perovskite is an antiferromagnet with Neel temperature $T_N = 100$ K [7]. Therefore, in the range of room temperatures, this orthorhombic $Pbnm$ phase is in the paramagnetic state and its small amount < 1 wt. % cannot affect the magnetic behavior of the LSMO-800 powder (see Fig. 2).

For determining the type of the particle size distribution function, the $La_{0.6}Sr_{0.4}MnO_3$ nanopowders with a minimum $t_{ann} = 800$ °C and a maximum $t_{ann} = 900$ °C annealing temperatures were selected. Analysis of raster SEM images along the particle contour, taking into account the scale factor, made it possible to plot the particle size distribution (see Fig. S3). The counting number for one sample exceeded 100. According to SEM images, the particles of the studied samples may suppose spherical-like. In addition, the particle size D was measured one by one manually and once within clear and defined margins of the particle.

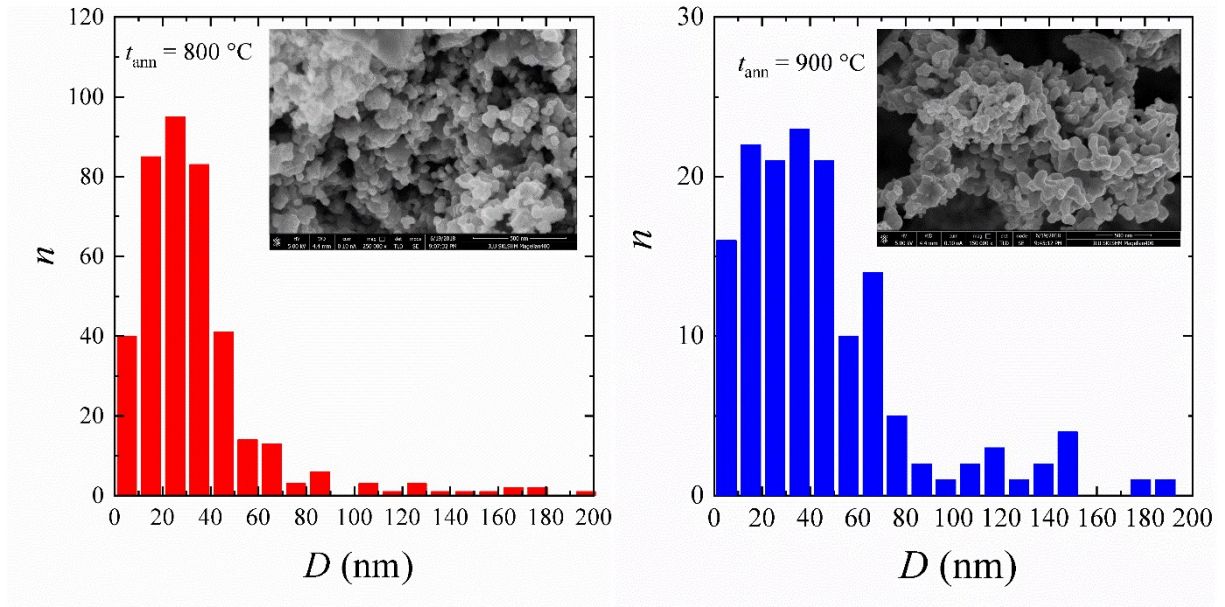


Fig. S3. Particle size distribution in the $\text{La}_{0.6}\text{Sr}_{0.4}\text{MnO}_3$ nanopowders with $t_{\text{ann}} = 800$ and $900 \text{ }^\circ\text{C}$ according to SEM images (inset).

The type of the distribution function $f = f(D)$ was selected among the three most frequently used functions: the Gaussian function (S2), the Lorentzian function (S3), and the LogNormal Distribution (S4):

$$f(x) = A \cdot \exp\left[-\frac{(x-x_0)^2}{2\sigma^2}\right], \quad (\text{S2})$$

$$f(x) = \frac{2A}{\pi} \cdot \frac{\sigma}{4 \cdot (x-x_0)^2 + \sigma^2}, \quad (\text{S3})$$

$$f(x) = \frac{A}{\sqrt{2\pi}\sigma x} \cdot \exp\left[-\frac{\left[\ln\frac{x}{x_0}\right]^2}{2\sigma^2}\right], \quad (\text{S4})$$

where A is the normalization constant; x_0 is the mathematical expectation, which in our case corresponds to the average particle size, $D_0 = x_0$; σ^2 is the dispersion, which for an ensemble of particles means the size dispersion of particles.

While approximating the experimental values of the number of particles by the functions of (S2)–(S4) (see Fig. S4), it was found that the smallest error in the deviation of the experimental data from the dependences (S2)–(S4) was observed for the Gaussian function (S2). The criterion for the

selection of the function (S2) was the highest approximation accuracy when the coefficient of determination R^2 takes the maximum value (see Table S4). All functions (S2)–(S4) were normalized by the condition $\int_0^{+\infty} f(x)dx = 1$ and their analytical form can be restored taking into account the parameters from Table S4.

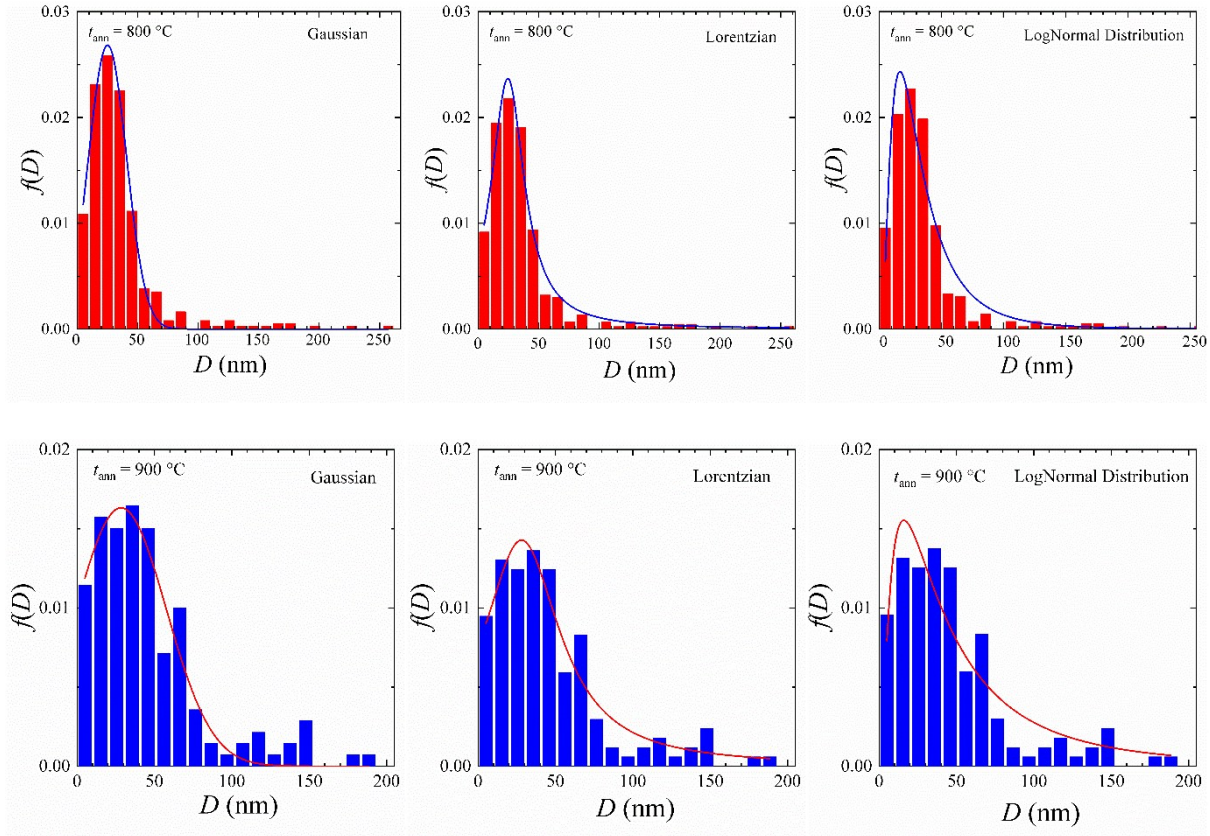


Fig. S4. Approximation of the experimental values of D in the $\text{La}_{0.6}\text{Sr}_{0.4}\text{MnO}_3$ nanopowders ($t_{\text{ann}} = 800$, and 900 °C) by the Gaussian function (SM2), the Lorentzian function (SM3), and the LogNormal Distribution function (SM4).

Table S4

The average particle size D_0 , dispersion σ , normalization constant A and determination coefficient R^2 upon approximation of the experimental values of D by the Gaussian, Lorentzian, and LogNormal Distribution functions in the $\text{La}_{0.6}\text{Sr}_{0.4}\text{MnO}_3$ nanopowders with $t_{\text{ann}} = 800$ and 900 °C.

$t_{\text{ann}},$ °C	Function	$D_0,$ nm	σ	A	R^2
800	Gaussian	25.2 ± 0.4	15.7 ± 0.5	0.0268	0.98930
	Lorentzian	24.7 ± 0.6	33.1 ± 1.9	1.2319	0.98052
	LogNormal	29.1 ± 1.8	32.7 ± 4.9	1.0000	0.93690
900	Gaussian	28.4 ± 2.7	29.3 ± 2.9	0.0163	0.93876
	Lorentzian	28.1 ± 2.2	60.3 ± 7.0	1.3535	0.93667
	LogNormal	42.4 ± 5.8	88.4 ± 29.4	0.9999	0.87623

According to SEM studies, LSMO powder consists of spherical particles with a visually determined average size of $D \sim 20 - 70$ nm. The particle size distribution function $f(D)$ was defined similarly to [8] and has the form of a Gaussian function (see Fig. S5):

$$f(D) = A \cdot \exp[-(D - D_0^{\text{SEM}})^2 / 2\sigma^2], \quad (\text{S5})$$

where A is the normalization constant, D_0^{SEM} is the average particle size; σ is the dispersion. In nanopowders, the average particle size slightly increases from $D_0^{\text{SEM}} = 25$ nm for LSMO-800 to 28 nm for LSMO-900. However, a large increase in dispersion is observed ~ 2 times from $\sigma = 15.7$ to 29.3 (see Table S4). This means that the powder with $t_{\text{ann}} = 800$ °C is more uniform in size. The analytical form of the Gaussian function $f(D)$ (see Table S4), taking into account the normalization condition $\int_0^\infty f(x)dx = 1$, allows to establish that the number of particles with a size $D \leq 50$ nm decreases from 94% (LSMO-800) to 72% (LSMO-900).

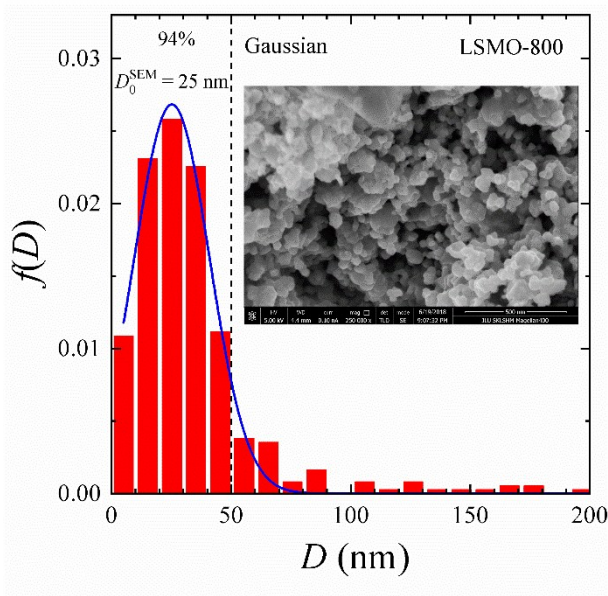


Fig. S5. Approximation of the particle size dispersion D in the LSMO-800 nanopowder by the Gaussian function $f(D)$ (D_0^{SEM} is the average particle size from SEM image, 94% of the particles have a size $D \leq 50$ nm).

According to the BET data, the specific surface area of the particles is $S_{\text{sa}} = 19.6778$ m²/g (LSMO-800), 12.7318 m²/g (LSMO-850) and 12.6440 m²/g (LSMO-900). For spherical particles, the area S_{sa} is related to the diameter D^{BET} by the equality:

$$S_{sa} = 6/(\rho_x D^{BET}), \quad (S6)$$

where ρ_x is the X-ray density, which is 6.349 g/cm³ (LSMO-800), 6.288 g/cm³ (LSMO-850), and 6.255 g/cm³ (LSMO-900). In the La_{0.6}Sr_{0.4}MnO₃ nanopowders with $t_{ann} = 800, 850, \text{ and } 900$ °C, the X-ray density ρ_x was calculated using XRD data (ESI2) according to the formula: $\rho_x = (Z \cdot M_0)/(V \cdot N_A)$, where $Z = 6$ is the number of formula units in the unit cell, $M_0 = 221.328$ g/mol is the molar mass of La_{0.6}Sr_{0.4}MnO₃, V is the volume of the unit cell; $N_A = 6.022 \cdot 10^{23}$ mol⁻¹ is the Avogadro's number. It was found from Equation (S6) that the D^{BET} size increases from 48.0 nm (LSMO-800) to 74.9 nm (LSMO-850) and 75.9 nm (LSMO-900) with an increase in the temperature t_{ann} . Table S5 shows that the average particle size of D^{CSR} and D_0^{SEM} according to XRD and SEM methods correlate well with each other. High values D^{BET} from the BET method can be associated with the adhesion of nanoparticles, which reduces the total surface area of the powder during the formation of a nitrogen monolayer in the BET method.

Table S5
X-ray density ρ_x , specific surface area S_{sa} , and average particle size according to XRD (D^{CSR}), SEM (D_0^{SEM}) and BET (D^{BET}) methods in LSMO nanopowders.

Powder	$\rho_x, \text{g/cm}^3$	D^{CSR}, nm	D_0^{SEM}, nm	$S_{sa}, \text{m}^2/\text{g}$	D^{BET}, nm
LSMO-800	6.349	20±1	25.2±0.4	19.6778	48.0
LSMO-850	6.288	26±1	–	12.7318	74.9
LSMO-900	6.255	30±1	28.4±2.7	12.6440	75.9

The conducted analysis of the phase composition, structure, morphology, and particle size allows to select the synthesized LSMO-800 powder as a single-phase quasi monodispersed powder with an average particle size $D_0 = 25$ nm for studying the multifunctionality of lanthanum-strontium manganite perovskite nanopowder.

ESI4

Magnetic properties of the LSMO-800

In the PM region, the total magnetic moment of manganese $\mu_{tot}(\text{Mn})$ can be obtained from the equation [9]:

$$\mu_{\text{tot}}(\text{Mn}) = \sqrt{x_1 \cdot \mu_{\text{Mn}^{3+}}^2 + x_2 \cdot \mu_{\text{Mn}^{4+}}^2}, \quad (\text{S7})$$

where x_1 and x_2 are the concentrations of Mn^{3+} and Mn^{4+} ions, respectively. In the ground state, the magnetic moments $\text{Mn}^{3+}(3d^4)$ with spin $S = 2$ and $\text{Mn}^{4+}(3d^3)$ with spin $S = 3/2$ are equal to $\mu_{\text{Mn}^{3+}} = 4.90\mu_{\text{B}}$ and $\mu_{\text{Mn}^{4+}} = 3.87\mu_{\text{B}}$, respectively [10]. Using Equation (S7) with $x_1 = 0.6$ and $x_2 = 0.4$, $\mu_{\text{tot}}(\text{Mn}) = 4.52 \mu_{\text{B}}$ is obtained. Additionally, in PM state, the Curie-Weiss law should be performed $\chi = C / (T - \Theta)$, where χ is the magnetic susceptibility, Θ is the paramagnetic Curie temperature, $C = N\mu_{\text{eff}}^2/(3k_{\text{B}})$ is the Curie constant, N is the number of paramagnetic manganese ions, μ_{eff} is the effective magnetic moment of manganese in Bohr magnetons μ_{B} . In the temperature range from 380 to 400 K, the linear dependence $\chi^{-1}(T)$ is approximated with high accuracy by the Curie–Weiss law (see Fig. S6) with $C = 0.009 \text{ emu} \cdot \text{K}/(\text{g} \cdot \text{Oe})$, $\Theta = 358 \text{ K}$ and $\mu_{\text{eff}}(\text{Mn}) = 3.96 \mu_{\text{B}}$. The deviation of the calculated $\mu_{\text{tot}}(\text{Mn}) = 4.52 \mu_{\text{B}}$ from the experimental $\mu_{\text{eff}}(\text{Mn}) = 3.96 \mu_{\text{B}}$ can be explained by the appearance of non-stoichiometry defects in the form of cation and anion vacancies, the concentration of which affects the charge, valence, and magnetic states of ions in perovskites containing $3d$ -ions of variable valence [11].

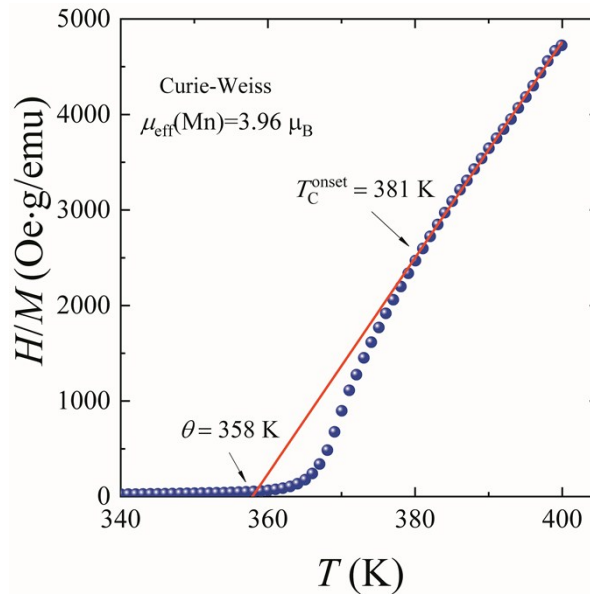


Fig. S6. An approximation of the inverse magnetic susceptibility $\chi^{-1}(T) = H/M(T)$ by the Curie law for the LSMO-800 nanopowder (Θ is the paramagnetic Curie temperature, $T_{\text{C}}^{\text{onset}}$ is the temperature

of the appearance of FM correlations, and $\mu_{\text{eff}}(\text{Mn})$ is the effective magnetic moment of manganese).

The field dependences $M(H)$ of randomly oriented FM ultrafine particles are well approximated by the law of the magnetization to saturation [12]:

$$M = M_s \left(1 - \frac{a}{H} - \frac{b}{H^2} - \frac{c}{H^3} \right) + \chi_d H, \quad (\text{S8})$$

where a , b , and c are constant coefficients; χ_d is the high-field susceptibility. Among the coefficients a , b , and c , only b depends on the saturation magnetization and magnetic anisotropy [13]. For rare-earth manganites with a cubic perovskite structure [14]:

$$b = \frac{1}{M_s^2} \left(\frac{8}{105} K_1^2 + \frac{4}{15} K_{\text{eff}}^2 \right),$$

where K_1 is the magnetocrystalline anisotropy constant, K_{eff} is the effective anisotropy constant that includes the shape anisotropy constant and the magnetostriction constant. For the systems with uniaxial anisotropy, the upper limit K_1 can be obtained from equality [12]:

$$K_1 = \left[\frac{15}{4} b M_s^2 \right]^{1/2}. \quad (\text{S9})$$

While approximating the isotherm $M(H)$ for $T = 4$ K by the dependence (S8) (see Fig. 3b), the coefficient $b = 67937 \text{ Oe}^2$ was obtained. Using equation (S9) with a saturation magnetization $M_s = 316.2 \text{ emu/cm}^3$, the value for magnetocrystalline anisotropy $K_1 = 1.60 \cdot 10^5 \text{ erg/cm}^3$ was obtained. The value of K_1 is in satisfactory agreement with $K_1 = 1.0 \cdot 10^5 \text{ erg/cm}^3$ for the similar composition $\text{La}_{0.75}\text{Sr}_{0.25}\text{MnO}_3$ [15].

The critical size for MNP is the $D_{\text{cr}}^{\text{SD}}$ when the particle transitions from the single-domain (SD) to the multidomain (MD) state [15]. The size of the $D_{\text{cr}}^{\text{SD}}$ depends on the magnetic hardness of the particle. The criterion of the magnetic hardness parameter is the parameter k [16]:

$$k = 2K_1/4\pi M_s^2. \quad (\text{S10})$$

Brown's rigorous approach [17], based on Kittel's estimation approach [18,19], establishes a criterion for magnetic hardness for spherical MNPs with uniaxial anisotropy:

$$k \ll 0.3562 \text{ for soft magnetic particles,} \quad (\text{S11})$$

$$k \geq 0.3562 \text{ for hard magnetic particles.} \quad (\text{S12})$$

Using the experimental values of K_1 and M_S , the value of the parameter $k = 0.254$ can be obtained. According to condition (S11), the LSMO-800 powder is magnetically soft. However, the value of the k is not much different from condition (S12) for magnetically hard particles with high coercivity. In [15,17], the critical sizes of $D_{\text{cr}}^{\text{SD}}$ and $D_{\text{cr}}^{\text{MD}}$ were obtained:

$$D_{\text{cr}}^{\text{SD}} = 7.211 \left(\frac{2A}{4\pi M_S^2} \right)^{1/2}, \quad (\text{CGS}), \quad (\text{S13})$$

$$D_{\text{cr}}^{\text{MD}} = \frac{9.0584 \cdot \left(\frac{2A}{4\pi M_S^2} \right)^{1/2}}{1 - 2.8075 \cdot \frac{2K_1}{4\pi M_S^2}}, \quad (\text{CGS}), \quad (\text{S14})$$

where A is the exchange hardness constant. For magnetically ordered crystals, the constant A is equal to [16]:

$$A = \frac{NJ_{\text{ex}}S^2}{a}, \quad (\text{CGS}), \quad (\text{S15})$$

where N is the number of magnetic ions in the unit cell; J_{ex} is the exchange integral; S is the spin quantum number of the magnetic ion; a is the lattice constant. For a simple cubic lattice with $N = 1$, the exchange integral J_{ex} , taking into account the influence of the second coordination sphere, is related to the Curie temperature T_C by the relation [20,21]:

$$J_{\text{ex}} = \frac{3k_B T_C}{ZS(S+1)}, \quad (\text{S16})$$

where $Z = 6$ is the number of nearest neighbors. In soft magnetic particles with the size $D_{\text{cr}}^{\text{SD}} < D < D_{\text{cr}}^{\text{MD}}$, the transition from SD to MD state occurs through the appearance of a vortex state (VS). The VS with closed lines of magnetization is a type of SD state. Using Equations (S13)–(S16), the values for the exchange hardness constant $A = 4.055 \cdot 10^{-7}$ erg/cm, the exchange integral $J_{\text{ex}} =$

$5.442 \cdot 10^{-15}$ erg, and the critical sizes $D_{cr}^{SD} = 58$ nm and $D_{cr}^{MD} = 136$ nm were obtained. For SD particles at $D \leq D_{cr}^{SPM}$, where D_{cr}^{SPM} is the critical size of the SPM state, their coercivity is $H_C = 0$. Using the expression $D_{cr}^{SPM} = [25k_B T / (\alpha K_1)]^{1/3}$ [16] (for spherical particles, the coefficient $\alpha = \pi/6$), the critical size $D_{cr}^{SPM} = 5$ nm at $T = 4$ K can be found for the LSMO-800 nanopowder.

ESI5

Additional electrochemical details

We used Hg/HgO or Ag/AgCl as the reference electrode for electrochemical measurements (calibrated with respect to RHE).

$$E_{RHE} = E_{Hg/HgO} + 0.921V \text{ (for 1 M KOH solution)}$$

$$E_{RHE} = E_{Hg/HgO} + 0.463V \text{ (for 1 M Na}_2\text{SO}_4 \text{ solution)}$$

The measurements were performed in a 1 M aqueous KOH or Na₂SO₄ electrolytes after purging with purity O₂ or Ar for at least 30 min.

ESI6

Electrochemical characteristics of the LSMO in 1 M KOH solution

The electrochemical tests of the manufactured LSMO anodes were carried out by CV (cyclic voltammetry), LSV (linear sweep voltammetry) and CP (chronopotentiometry) in 1 M KOH aqueous solution. CV curves within the potential range from 0.2 to 1.6 V (vs RHE) are similar for all the studied electrodes. As an example, Figure S7 shows the CVM curves of the LSMO-800 electrode at different scan rates. In all cases, two reductive peaks appears at approximately 0.45 and 0.85 V, which could be ascribed to the Mn(III)/Mn(II) and Mn(IV)/Mn(III) couples of LSMO. A similar phenomenon was also observed in previous reports for manganese perovskites [22-24].

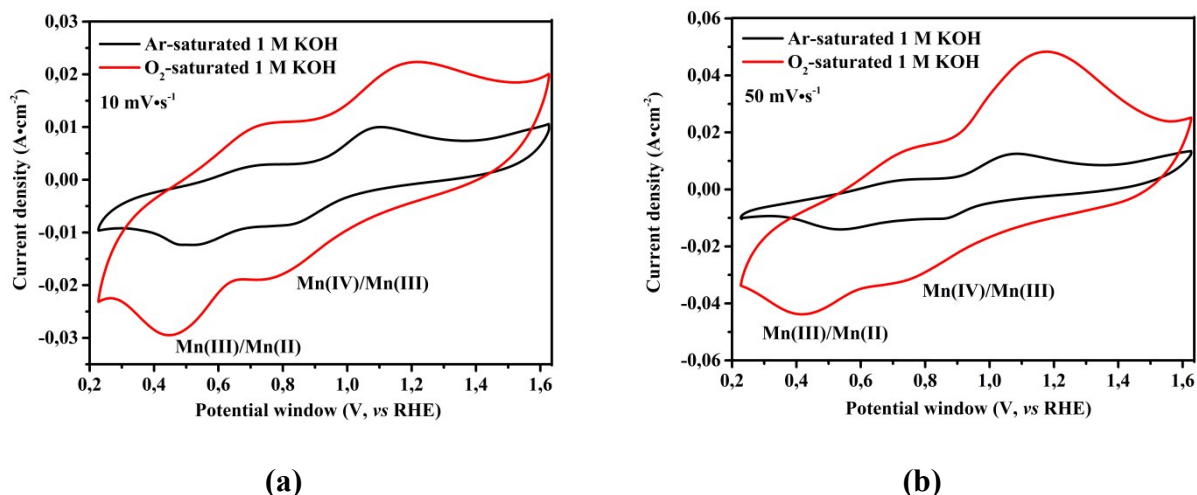


Fig. S7. CV curves of LSMO-800 electrodes in Ar-saturated and O₂-saturated 1 M KOH at a sweep rate of 10 mV·s⁻¹ (a) and 50 mV·s⁻¹ (b).

OER activity was evaluated using the LSV test. Within 1.6 V (vs RHE), the highest current densities are found for the LSMO-800 anode (Fig. S8(a)). In this case (the anode current density reach 6–7 mA·cm⁻²) gas bubbles are emitted from the electrode surface. OER the activity is much lower for electrodes based on the LSMO-850 and LSMO-900. As example, the LSMO-900 electrode shows a current density of only 1.4 mA·cm⁻² at a voltage of 1.6 V (Fig. S8(b)). Thus, enhanced OER activity results mainly from the presence of LSMO nanoparticles with smaller size.

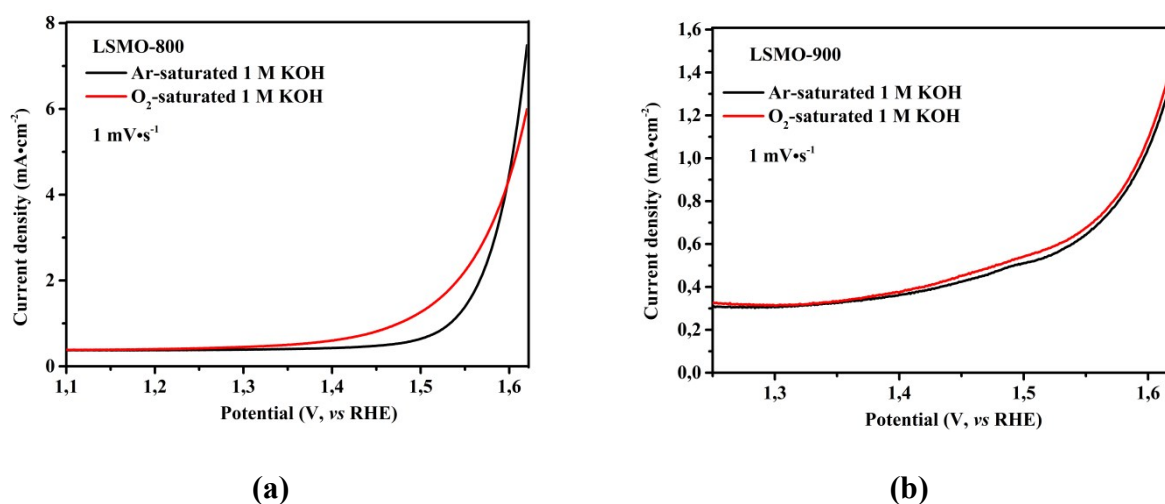


Fig. S8. LSV curves of LSMO-800 (a) and LSMO-900 (b) electrodes in Ar-saturated and O₂-saturated 1 M KOH at a sweep rate of 1 mV·s⁻¹ (iR-compensation 90%).

In the next step of the study, we performed a CP test to determine the stability of the LSMO catalysts with increasing current density. Chronopotentiometry was carried out at a value of

10 mA·cm⁻². As shown in Fig. S9(a), for this value of current density, the potential increases strong and already in the first 10 minutes exceeds 1.8 V. As a result, intense release of gas bubbles occurs and mechanical destruction of the electrodes is observed (Fig. S9(b)). Corrosion of the electrodes is accompanied by staining of the electrolyte in purple and green (leaching of the Mn^{VII}O₄⁻ and Mn^{VI}O₄²⁻). Thus, LSMO type electrocatalysts are limited for using in an alkaline electrolyte by voltage window value (with a limit lower than 1.8 V).

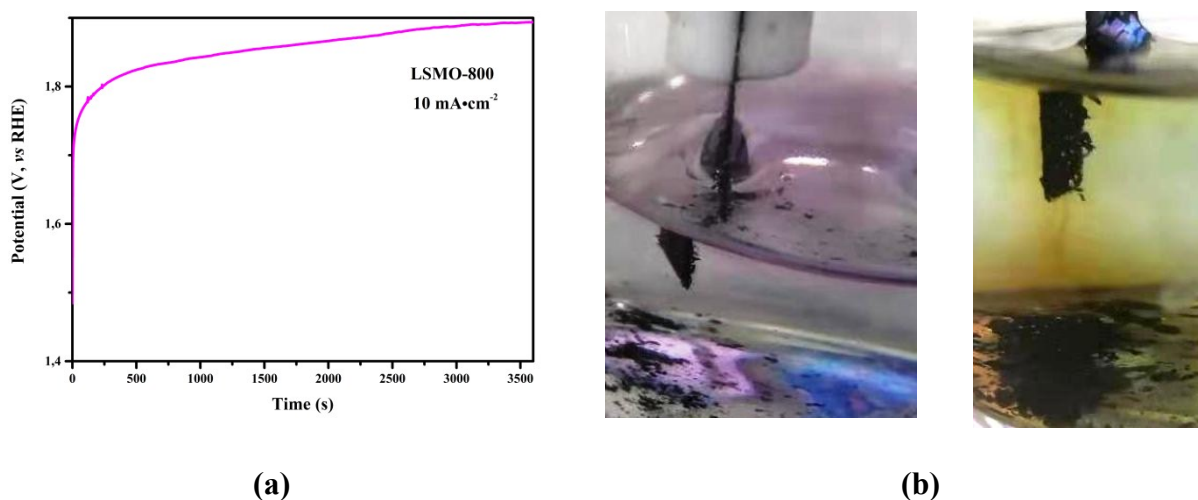


Fig. S9. Chronopotentiometry test of LSMO-800 catalyst at the current density of 10 mA·cm⁻²: (a) CP curve; (b) photo of electrode corrosion.

ESI7

Electrochemical characteristics of the LSMO in 1 M Na₂SO₄ solution

Equivalent circuit

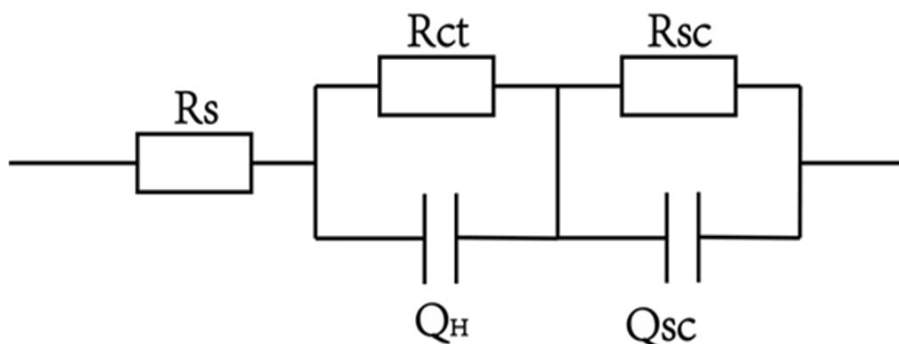


Fig. S10. The equivalent scheme for EIS measurement: R_s – solution resistance, R_{ct} – the resistance of electron transfer on a anode; Q_H – constant phase element (CPE), represents Helmholtz layer capacitance; Q_{sc} – constant phase element (CPE), represents space charge layer capacitance; R_{sc} is the space charge separation resistance Q is the constant phase element (CPE).

Since the charge transport and transfer process is considered to be normally much faster in the bulk than that in the semiconductor-electrolyte interface, the low frequency response has been assigned to the semiconductor-electrolyte charge transfer behavior (R_{ct} and Q_H) while the high frequency response has been designated to the behavior in the semiconductor bulk (R_{SC} and Q_{SC}) correspondingly.

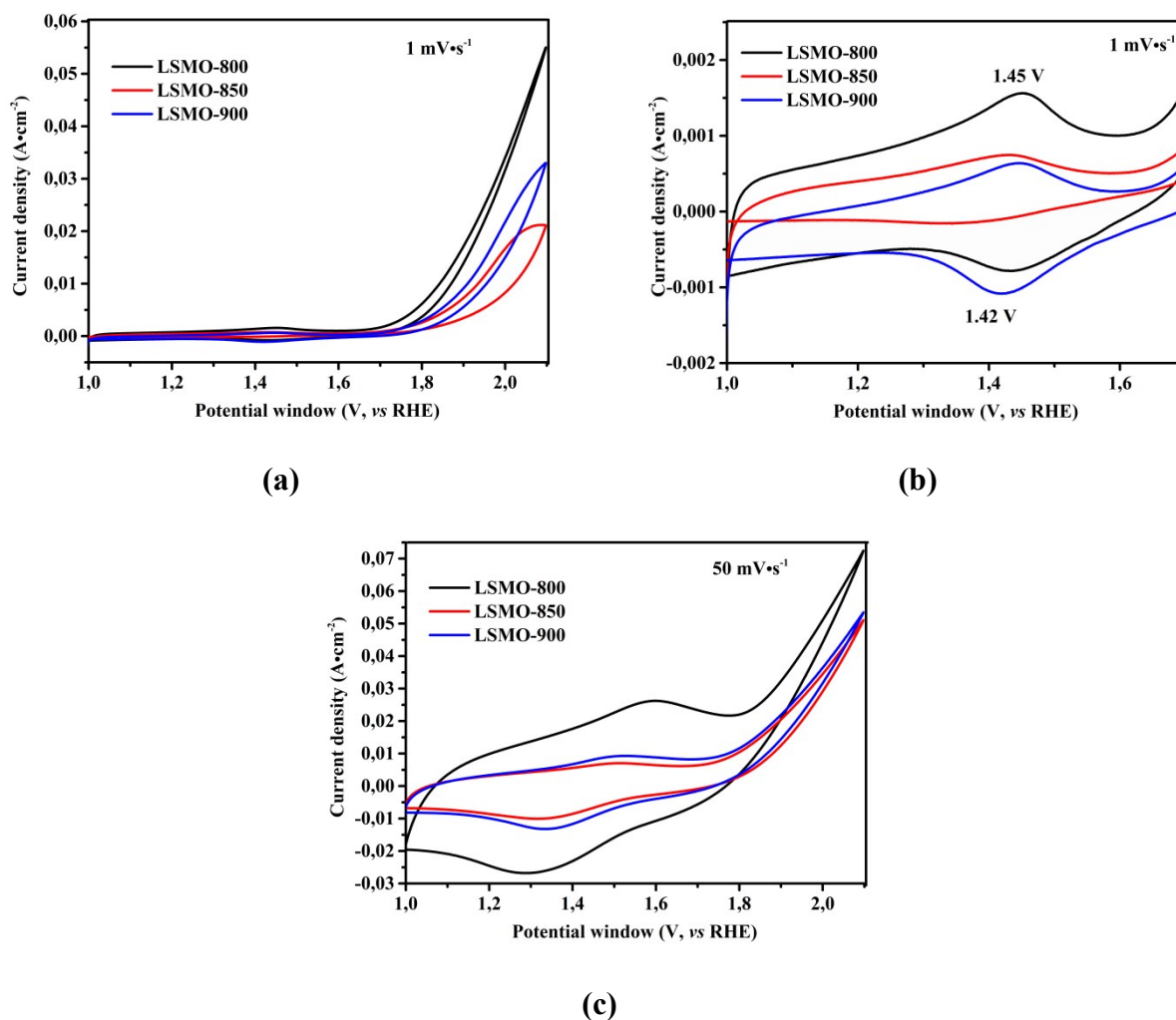


Fig. S11. CV curves of LSMO electrodes in 1 M Na_2SO_4 at different sweep rate: (a) $1 mV \cdot s^{-1}$; (b) $1 mV \cdot s^{-1}$ for within voltages from 1,0 to 1,7 ; (c) $50 mV \cdot s^{-1}$.

References

- [1] A.L. Patterson, The Scherrer Formula for X-Ray Particle Size Determination, *Phys. Rev.* 56 (1939) 978-982.
- [2] B.E. Warren, X-Ray Diffraction Methods, *J. Appl. Phys.* 12 (1941) 375-384.
- [3] J.A.M. Van Roosmalen, P. van Vlaanderen, E.H.P. Cordfunke, W.L. IJdo, D.J.W. IJdo, Phases in the Perovskite-Type $LaMnO_{3+\delta}$ Solid Solution and the La_2O_3 - Mn_2O_3 Phase Diagram, *J. Solid State Chem.* 114 (1995) 516-523.

- [4] A.V. Pashchenko, V.P. Pashchenko, V.K. Prokopenko, Yu.F. Revenko, Yu.S. Prylipko, N.A. Ledenev, G.G. Levchenko, V.P. Dyakonov, H. Szymczak, Influence of structure defects on functional properties of magnetoresistance $(\text{Nd}_{0.7}\text{Sr}_{0.3})_{1-x}\text{Mn}_{1+x}\text{O}_3$ ceramics, *Acta Material.* 70 (2014) 218–227.
- [5] A. Pashchenko, V. Pashchenko, V. Prokopenko, Yu. Revenko, A. Mazur, V. Burchovetskiy, V. Turchenko, M. Liedienov, V. Pitsyuga, G. Levchenko, V. Dyakonov, H. Szymczak, The role of structural and magnetic inhomogeneities in the formation of magneto-transport properties of the functional magnetoresistance $\text{La}_{0.6-x}\text{Sm}_x\text{Sr}_{0.3}\text{Mn}_{1.1}\text{O}_{3-d}$ ceramics, *J. Magn. Magn. Mater.* 416 (2016) 457–465.
- [6] F. Zheng, L.R. Pederson, Phase Behavior of Lanthanum Strontium Manganites, *J. Electrochem. Society.* 146 (1999) 2810-2816.
- [7] A. Zouari, C. Boudaya, E. Dhahri, Effect of the Oxygen Deficiency on the Structural, Magnetic and Electrical Properties in Perovskite-Like $\text{La}_{0.6}\text{Sr}_{0.4}\text{MnO}_{3-d}$, *Phys. Stat. Sol. (a).* 188 (2001) 1177–1186.
- [8] Z. Wei, Q. Li, N. Liedienov, G. Levchenko, A. Pashchenko, I. Fesych, E. Zubov, I. Zatovskyi, A. Voznyak, V. Pitsyuga, D. Chernov, Morphology and Functional Properties of Magnetic Nanoparticles of Lanthanum-Strontium Manganites. 2019 IEEE 39th International Conference on Electronics and Nanotechnology (ELNANO), APRIL 16-18, 2019 Kyiv, Ukraine. – p. 850. – P. 326 – 329.
- [9] A.D. Souza, P.D. Babu, S. Rayaprol, M.S. Murari, L.D. Mendonca, Size control on the magnetism of $\text{La}_{0.7}\text{Sr}_{0.3}\text{MnO}_3$, *J. Alloys Compd.* 797 (2019) 874-882.
- [10] V. Dyakonov, A. Slawska-Waniewska, N. Nedelko, E. Zubov, V. Mikhaylov, K. Piotrowski, A. Szytula, S. Baran, W. Bazela, Z. Kravchenko, P. Aleshkevich, A. Pashchenko, K. Dyakonov, V. Varyukhin, H. Szymczak, Magnetic, resonance and transport properties of nanopowder of $\text{La}_{0.7}\text{Sr}_{0.3}\text{MnO}_3$ manganites, *J. Magn. Magn. Mater.* 322 (2010) 3072–3079.

- [11] A.V. Pashchenko, N.A. Liedienov, Q. Li, D.D. Tatarchuk, V.A. Turchenko, I.I. Makoed, V.Ya. Sycheva, A.V. Voznyak, V.P. Kladko, A.I. Gudimenko, Y.V. Didenko, A.T. Kozakov, G.G. Levchenko, Structure, non-stoichiometry, valence of ions, dielectric and magnetic properties of single-phase $\text{Bi}_{0.9}\text{La}_{0.1}\text{FeO}_{3-\delta}$ multiferroics, *J. Magn. Magn. Mater.*, 483 (2019) 100–113.
- [12] D.H. Manh, P.T. Phong, T.D. Tung, D.N.H. Nam, L.V. Hong, N.X. Phuc, Size effects and interactions in $\text{La}_{0.7}\text{Ca}_{0.3}\text{MnO}_3$ nanoparticles, *J. Alloys Compd.* 509 (2011) 1373-1377.
- [13] H. Yang, Z. Wang, L. Song, M. Zhao, J. Wang, H. Luo, A study on the coercivity and the magnetic anisotropy of the lithium ferrite nanocrystallite, *J. Phys. D: Appl. Phys.* 29 (1996) 2574–2578.
- [14] D.H. Manh, P.T. Phong, P.H. Nam, D.K. Tung, N.X. Phuc, In-Ja Lee, Structural and magnetic study of $\text{La}_{0.7}\text{Sr}_{0.3}\text{MnO}_3$ nanoparticles and AC magnetic heating characteristics for hyperthermia applications, *Physica B.* 444 (2014) 94-102.
- [15] Y.O. Tykhonenko-Polishchuk, A.I. Tovstolytkin, On the Critical Size of the Transition of a Ferromagnet into a Single-Domain State. *J. Nano- Electron. Phys.* 9 (2017) 02028-1-02028-17.
- [16] A.P. Guimaraes, Nanoscience and technology. Principles of Nanomagnetism. s.l. : Springer, Berlin, Heidelberg, 2009. p. 221.
- [17] W.F. Brown, The Fundamental Theorem of Fine Ferromagnetic Particle Theory, *J. Appl. Phys.* 39 (1968) 993 - 994.
- [18] C. Kittel, Theory of the Structure of Ferromagnetic Domains in Films and Small Particles, *Phys. Rev.* 70 (1946) 965-971.
- [19] C. Kittel, Physical Theory of Ferromagnetic Domains. *Rev. Mod. Phys.* 21 (1949) 541-591.
- [20] P.R. Weiss, The Application of the Bethe-Peierls Method to Ferromagnetism. *Phys. Rev.* 74 (1948) 1493-1504.
- [21] S. Tikadzumi, Physics of Ferromagnetism. Magnetic Properties and Practice Applications. Translated into Russian under the title *Fizika ferromagnetizma. Magnitnye kharakteristiki i prakticheskie primeneniya*, Moscow: Mir, 1987.

- [22] M. Risch, K.A. Stoerzinger, S. Maruyama, W.T. Hong, I. Takeuchi, Y. Shao-Horn, $\text{La}_{0.8}\text{Sr}_{0.2}\text{MnO}_{3-\delta}$ Decorated with $\text{Ba}_{0.5}\text{Sr}_{0.5}\text{Co}_{0.8}\text{Fe}_{0.2}\text{O}_{3-\delta}$: A Bifunctional Surface for Oxygen Electrocatalysis with Enhanced Stability and Activity, *J. Am. Chem. Soc.* 136 (2014) 5229–5232.
- [23] J. Scholz, M. Risch, K.A. Stoerzinger, G. Wartner, Y. Shao-Horn, C. Jooss, Rotating Ring–Disk Electrode Study of Oxygen Evolution at a Perovskite Surface: Correlating Activity to Manganese Concentration, *J. Phys. Chem. C* 120 (2016) 27746–27756.
- [24] Y. Yang, W. Yin, S. Wu, X. Yang, W. Xia, Y. Shen, Y. Huang, A. Cao, Q. Yuan, Perovskite-Type LaSrMnO Electrocatalyst with Uniform Porous Structure for an Efficient Li-O_2 Battery Cathode, *ACS Nano* 10 (2016) 1240-1248.